Supporting Information

Two-dimensional amorphous iridium cobalt oxide for acidic oxygen evolution reaction

*Da Liu [a], Yue Wang [a], Jiarui Zhu[b], xuewei Gu[b], Hao Yang *[b], Yutian Xiong [a], Mingwang Shao *[b] and Qi Shao*[a]*

Table of Contents

1. **Experimental Procedures.**
2. **Figure S1.** (a) SEM image of IrO_2/Co_3O_4. (b) XRD pattern of IrO_2/Co_3O_4. (c) EDS image of IrO_2/Co_3O_4.
3. **Figure S2.** (a) SEM image of IrO_2. (b) XRD pattern of IrO_2. (c) EDS image of IrO_2.
4. **Figure S3.** (a) SEM image of Co_3O_4. (b) XRD pattern of Co_3O_4. (c) EDS image of Co_3O_4.
5. **Figure S4.** EDS image of Am-$IrCo_5O_x$.
6. **Figure S5.** (a) SEM image of Am-$IrCo_3O_x$. (b) TEM image of Am-$IrCo_3$Ox. (c) STEM-EDS element mapping images of Am-$IrCo_3O_x$. (d) XRD pattern of Am-$IrCo_3$Ox. (e) EDS image of Am-$IrCo_3O_x$.
7. **Figure S6.** (a) SEM image of Am-$IrCo_4O_x$. (b) TEM image of Am-$IrCo_4$Ox. (c) STEM-EDS element mapping images of Am-$IrCo_4O_x$ (d) XRD pattern of Am-$IrCo_4O_x$. (e) EDS image of Am-$IrCo_4O_x$.
8. **Figure S7.** (a) SEM image of Am-$IrCo_6O_x$. (b) TEM image of Am-$IrCo_6$Ox. (c) STEM-EDS element mapping images of Am-$IrCo_6O_x$ (d) XRD pattern of Am-$IrCo_6O_x$. (e) EDS image of Am-$IrCo_6O_x$.
9. **Figure S8.** (a) SEM image of Am-$IrCo_7O_x$. (b) TEM image of Am-$IrCo_7$Ox. (c) STEM-EDS element mapping images of Am-$IrCo_7O_x$ (d) XRD pattern of Am-$IrCo_7O_x$. (e) EDS image of Am-$IrCo_7O_x$.
10. **Figure S9.** EPR spectra of Am-$IrCo_5O_x$ and IrO_2/Co_3O_4.
11. **Figure S10.** Calibration of the saturated calomel electrode (SCE) electrode with respect to reversible hydrogen electrode (RHE) in 0.5 M H_2SO_4 aqueous electrolytes bubbled with pure hydrogen gas at room temperature. Scan rate: 1 mV s^{-1}.
12. **Figure S11.** Reproducibility experiments for (A) Am-$IrCo_5O_x$, (b) IrO_2/Co_3O_4 and (c) C-IrO_2.
13. **Figure S12.** Measured CVs of (a) Am-$IrCo_5O_x$, (b) IrO_2/Co_3O_4 (c) IrO_2 in 0.5 M H_2SO_4 electrolyte with a potential range, measured at the scan rates of 5, 10, 15, 20, ,25, 30 and 35 mV s^{-1}. The current densities were obtained from the double layer charge/discharge curves.
14. **Figure S13.** C_{dl} plots obtained from the polarization curves of Am-$IrCo_5O_x$, IrO_2/Co_3O_4 and C-IrO_2.
15. **Figure S14.** Nyquist diagrams of Am-$IrCo_5O_x$, IrO_2/Co_3O_4 and C-IrO_2. The curves were the fitting result using the equivalent circuit shown in the illustration.
16. **Figure S15.** (a) SEM image and (b) TEM image of Am-$IrCo_5O_x$ after 122 hours stability test. (c) XRD of Am-$IrCo_5O_x$ after 122 hours stability test.

17. **Figure S16.** Chronopotentiometry test of Am-$IrCo_5O_x$, IrO_2/Co_3O_4 and C-IrO_2 at the current density of 50 mA cm^{-2}.
18. **Figure S17.** Measured CVs of (a) Am-$IrCo_3O_x$, (b) Am-$IrCo_4O_x$, (c) Am-$IrCo_6O_x$, (d) Am-$IrCo_7O_x$ in 0.5 M H_2SO_4 electrolyte with a potential range: 5, 10, 15, 20, 25, 30 and 35 mV s^{-1}. The current densities were obtained from the double layer charge/discharge curves.
19. **Figure S18.** C_{dl} plots obtained from the polarization curves of Am-$IrCo_5O_x$, Am-$IrCo_3O_x$, Am-$IrCo_4O_x$, Am-$IrCo_6O_x$, and Am-$IrCo_7O_x$.
20. **Figure S19.** Reproducibility experiments for (A) Am-$IrCo_4O_x$, (b) Am-$IrCo_3O_x$, (c) Am-$IrCo_6O_x$ and (d) Am-$IrCo_7O_x$.
21. **Figure S20.** (a) The IR spectrum of Am-$IrCo_5O_x$, IrO_2/Co_3O_4, and Co_3O_4. (b) The IR spectrum of Am-$IrCo_5O_x$, Am-$IrCo_7O_x$, Am-$IrCo_6O_x$, Am-$IrCo_4O_x$, and Am-$IrCo_3O_x$.
22. **Figure S21.** Raman of Am-$IrCo_5O_x$, Co_3O_4 and IrO_2.
23. **Figure S22.** The optimized structures of all states for OER on Ir sites on Am-$IrCo_5O_x$.
24. **Figure S23.** The optimized structures of all states for OER on Co sites on Am-$IrCo_5O_x$.
25. **Figure. S24.** Schematic representation of the OER mechanism on Ir sites on Am-$IrCo_5O_x$ surface: (a) LOM and (b) AEM. Schematic representation of the OER mechanism on Co sites on Am-$IrCo_5O_x$ surface: (c) LOM and (d) AEM.
26. **Table S1.** Comparisons of overpotential of catalysts with different ratios of Ir and Co.
27. **Table S2.** ICP-MS test of Am-$IrCo_5O_x$ during the 122 hours long-term stability test to check the concentration of dissolved Ir and Co in the electrolyte.
28. **Table S3.** Comparisons of OER performance for various Ir-based electrocatalysts.
29. **Table S4**. Grand free energy of mechanistic reactions steps under different reaction mechanisms on Ir sites on Am-$IrCo_5O_x$.
30. **Table S5**. Grand free energy of mechanistic reactions steps under different reaction mechanisms on Ir sites on Am-$IrCo_5O_x$.

Experimental Procedures

Chemicals

Iridium trichloride ($IrCl_3$, 99.9%) were purchased from Alfa Aesar. cobalt chloride hexahydrate ($CoCl_2·6H_2O$) purchased from China National Pharmaceutical Group Chemical Reagent Co., Ltd. (Shanghai, China). sodium hydroxide (NaOH) purchased from China National Pharmaceutical Group Chemical Reagent Co., Ltd. (Shanghai, China). Nafion was purchased from Aldrich. The water was processed through an ultra-pure purification system (Aqua Solutions).

Synthesis of Am-$IrCo_5O_x$

Weigh 2.89 mg (0.01 mmol) of $IrCl_3·6H_2O$, 11.89 mg (0.05 mmol) $CoCl_2·6H_2O$ and 591 mg of NaOH and grind them evenly in a mortar. After grinding, place the powdered mixture into the porcelain boat. The calcination temperature and time are 400 ^oC and 2 h, and the heating rate is 10 ^oC/min.

Synthesis of Am-$IrCo_3O_x$

Weigh 2.89 mg (0.01 mmol) of $IrCl_3$, 7.14 mg (0.03 mmol) $CoCl_2·6H_2O$ and 401.2 mg of NaOH and grind them evenly in a mortar. After grinding, place the powdered mixture into the porcelain boat. The calcination temperature and time are 400 ^oC and 2 h, and the heating rate is 10 ^oC/min.

Synthesis of Am-$IrCo_4O_x$

Weigh 2.89 mg (0.01 mmol) of $IrCl_3$, 9.52 mg (0.04 mmol) $CoCl_2·6H_2O$ and 496.4 mg of NaOH and grind them evenly in a mortar. After grinding, place the powdered mixture into the porcelain boat. The calcination temperature and time are 400 ^oC and 2 h, and the heating rate is 10 ^oC/min.

Synthesis of Am-$IrCo_6O_x$

Weigh 2.89 mg (0.01 mmol) of $IrCl_3$, 14.28 mg (0.06 mmol) $CoCl_2·6H_2O$ and 686.8 mg of NaOH and grind them evenly in a mortar. After grinding, place the powdered mixture into the porcelain boat. The calcination temperature and time are 400 ^oC and 2 h, and the heating rate is 10 ^oC/min.

Synthesis of Am-$IrCo_7O_x$

Weigh 2.89 mg (0.01 mmol) of $IrCl_3$, 16.66 mg (0.07 mmol) $CoCl_2·6H_2O$ and 782 mg of NaOH and grind them evenly in a mortar. After grinding, place the powdered mixture into the porcelain boat. The calcination temperature and time are 400 ^oC and 2 h, and the heating rate is 10 ^oC/min.

Fabrication of IrO_2/Co_3O_4.

Commercial iridium oxide (IrO_2) and commercial cobalt tetraoxide (Co_3O_4) were mixed in 5 ml of water at an atomic ratio of 1 : 5, uniformly sonicated for 30 min, and dried.

Characterization

Crystal structure of the catalysts were characterized by X-ray powder diffraction (XRD, Philips X'pert PRO MPD diffractometer) with a Cu Kα radiation source (λ = 0.15406 nm). Transmission electron microscopy (TEM), high-angle annular dark-field scanning transmission electron microscopy (HAADF-STEM) and STEM energy-dispersive X-ray spectroscopy (HAADF-STEM-EDX) were conducted on a FEI Tecnai F20 TEM at an accelerating voltage of 200 kV. The morphology and size of the nanocrystals were determined by TEM (Hitachi, HT7700) at 120 kV. The continuous ultrathin carbon layer on a holey carbon/formvar support film were purchased from Zhongjingkeyi (Beijing) Film Technology Co., LTD. The surface terrain height of the nanosheets was measured by AFM (Bruker Dimension Icon). X-ray photoelectron spectroscopy (XPS) analysis was studied on Thermo Scientific ESCALAB 250 XI X-ray photoelectron spectrometer. All data were calibrated by the C 1s peak of 284.8 eV.

Electrochemical measurements

All electrochemical experiments were conducted on CHI660E electrochemical workstation (Shanghai Chenhua, China). All the experiments were carried out at room temperature. The traditional three electrode system is adopted. Glass carbon electrode (GCE, area: 0.196 cm^2) or carbon paper (1 × 1 cm^2) was used as the working electrode, saturated calomel electrode used as the reference electrode, and carbon rod was used as the counter electrode. OER measurements were carried out in an oxygen saturated 0.5 M H_2SO_4 electrolyte. The iR correction is 95% and R is the ohmic resistance caused by the electrolyte/contact resistance of the device. The scanning speed is 5 mV s^{-1} for LSV measurement. All potentials measured were calibrated to RHE using the following equation: E (RHE) = E (SCE) + 0.241 V + 0.0591pH. 400 μL Isopropanol and 10 μL 0.5 wt% Nafion solution were mixed with 1 mg catalyst and subjected to ultrasonic treatment to form homogeneous catalyst ink. 25 μL the ink is dispersed on GCE and dried naturally for test. Each catalyst undergoes at least three catalytic activity and durability tests.

DFT simulation methods

DFT calculations were carried out using the VASP software (version 5.4.4) with the Perdew-Burke-Ernzerhof flavour of DFT. Projective augmentation wave method is used to explain the nucleation valence interaction. The kinetic energy cutoff value of plane wave expansion was set to 400 eV, and the reciprocal space was sampled by the Monkhorst-Pack scheme of $3\times3\times1$ grid. Finer K spacing does not produce more accurate prediction basing on our benchmark calculation. Spin polarization does not have an appreciable effect on the overall energies and is not included in the calculations to reduce computational demands. The vacuum layer was set to 20 Å to

prevent interactions between two neighboring surfaces. The energy cut-off is set to 400 eV. Larger energy cut-off does not produce more accurate prediction basing on our benchmark calculation. The minimization was considered converged when all the atomic force was are smaller than 0.01 eV/Å. DFT-D3 method with Becke-Jonson damping was included in the calculations to describe van der Waals (vdW) interactions. The free energies of all intermediates are defined as $G = E_0 + E_{ZPE} - TS$, where E_0, E_{ZPE}, T and S represent the calculated ground state energy, zero-point energy, temperature (298 K) and the entropy, respectively. The correction mentioned above is achieved by using VASPKIT code to post-process the data computed by VASP. The Molecular Dynamics (MD) simulations were performed in the NVE ensembles. We used a 1.0 fs time step in the Molecular Dynamics (MD) simulations with the hydrogen mass set to 2 atomic mass units. These MD simulations used only the gamma point of the Brillouin zone with no consideration of symmetry. For MD equilibrations, the velocities are scaled to the target temperature every 20 steps. For MD productions, the time integration is Nose-Hoover style non-Hamiltonian equations of motion with a timespan of 200 fs. We constructed the Am-$IrCo_5O_x$ structure started from the rutile-IrO_2, which is the stable phase of IrO_2. For the layered $Ir_xCo_{1-x}O_2$ periodic model, the IrO_2 (111) surface was constructed by a 5×5 supercell slab model with three layers, then the ~5/6 Ir were replaced by Co to reach the optimum ratio of as-synthesized catalyst, and the bottom two layers were fixed during the geometry optimization. The amorphous structure was then obtained by Monte Carlo Simulated Annealing (MC) process.

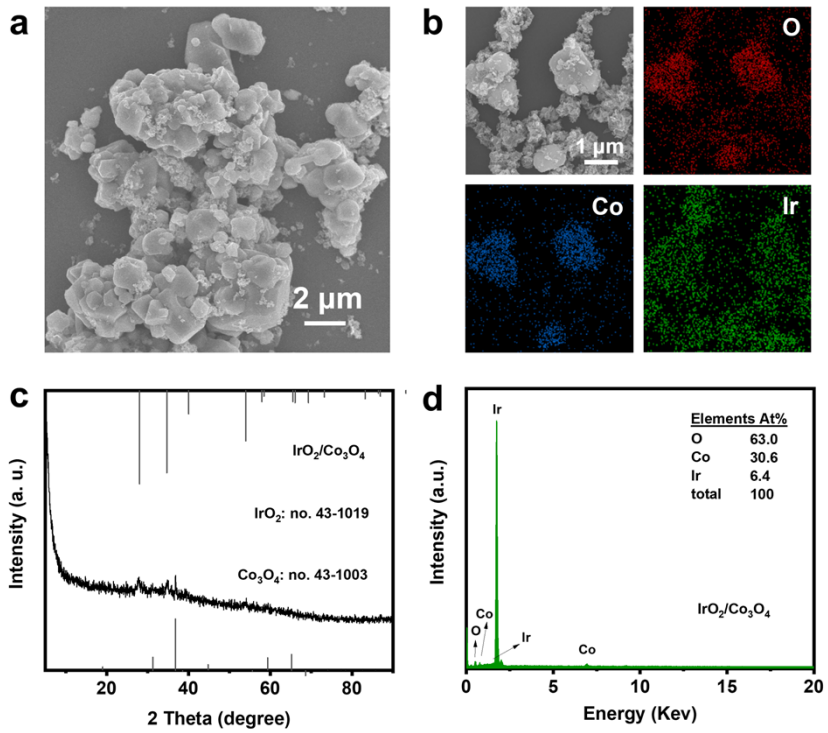

Figure S1. (a) SEM image of IrO_2/Co_3O_4. (b) XRD pattern of IrO_2/Co_3O_4. (c) EDS image of IrO_2/Co_3O_4.

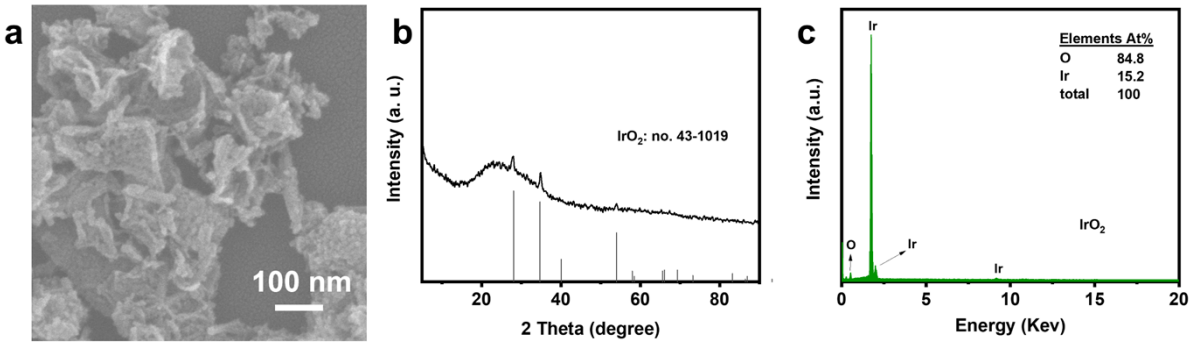

Figure S2. (a) SEM image of IrO_2. (b) XRD pattern of IrO_2. (c) EDS image of IrO_2.

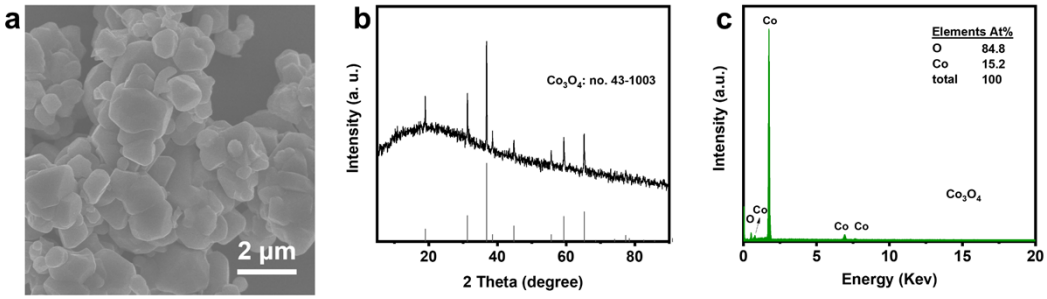

Figure S3. (a) SEM image of Co_3O_4. (b) XRD pattern of Co_3O_4. (c) EDS image of Co_3O_4.

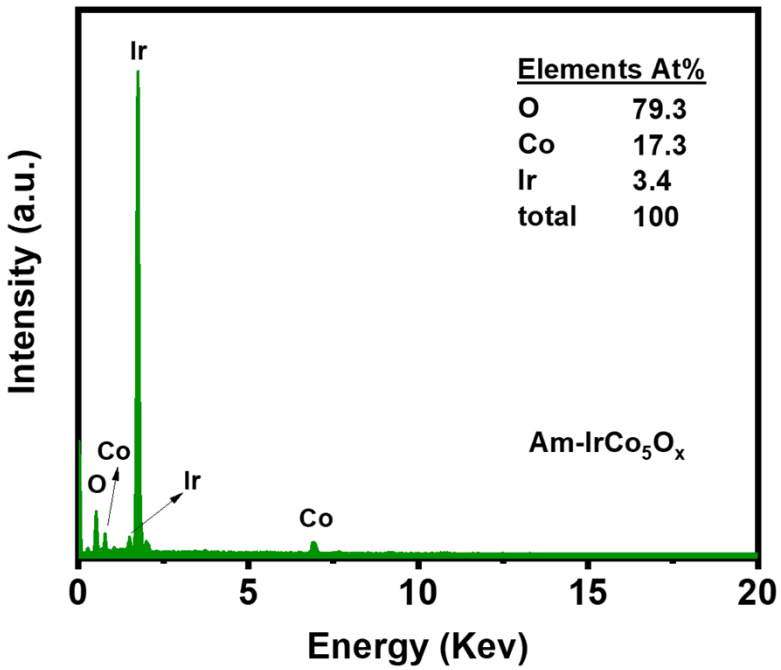

Figure S4. EDS spectrum of Am-$IrCo_5O_x$.

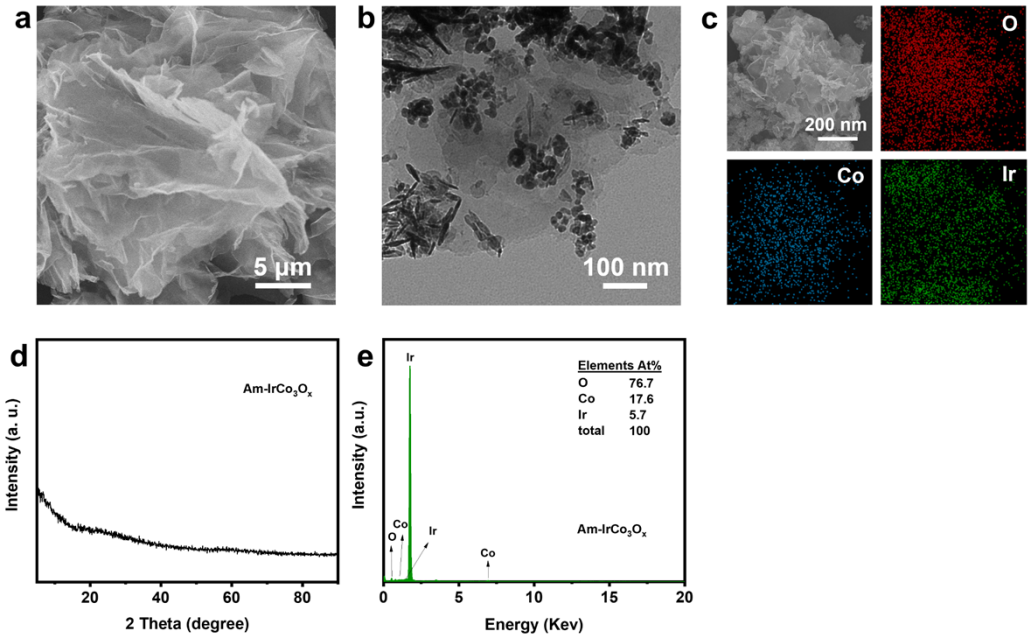

Figure S5. (a) SEM image of Am-$IrCo_3O_x$. (b) TEM image of Am-$IrCo_3$Ox. (c) STEM-EDS element mapping images of Am-$IrCo_3O_x$. (d) XRD pattern image of Am-$IrCo_3$Ox. (e) EDS image of Am-$IrCo_3O_x$.

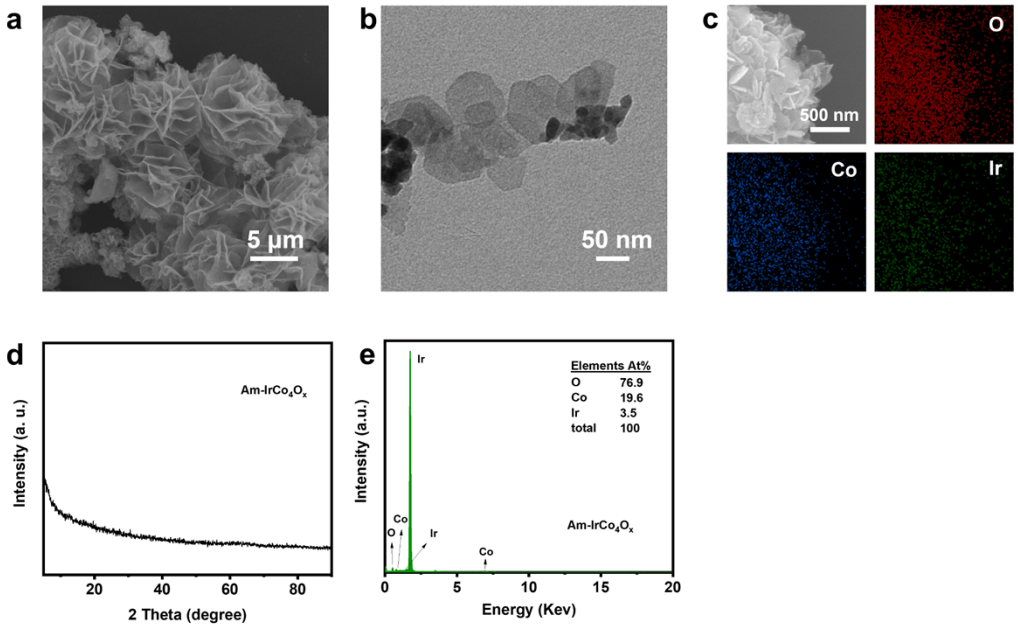

Figure S6. (a) SEM image of Am-$IrCo_4O_x$. (b) TEM image of Am-$IrCo_4$Ox. (c) STEM-EDS element mapping images of Am-$IrCo_4O_x$. (d) XRD pattern image of Am-$IrCo_4O_x$. (e) EDS image of Am-$IrCo_4O_x$.

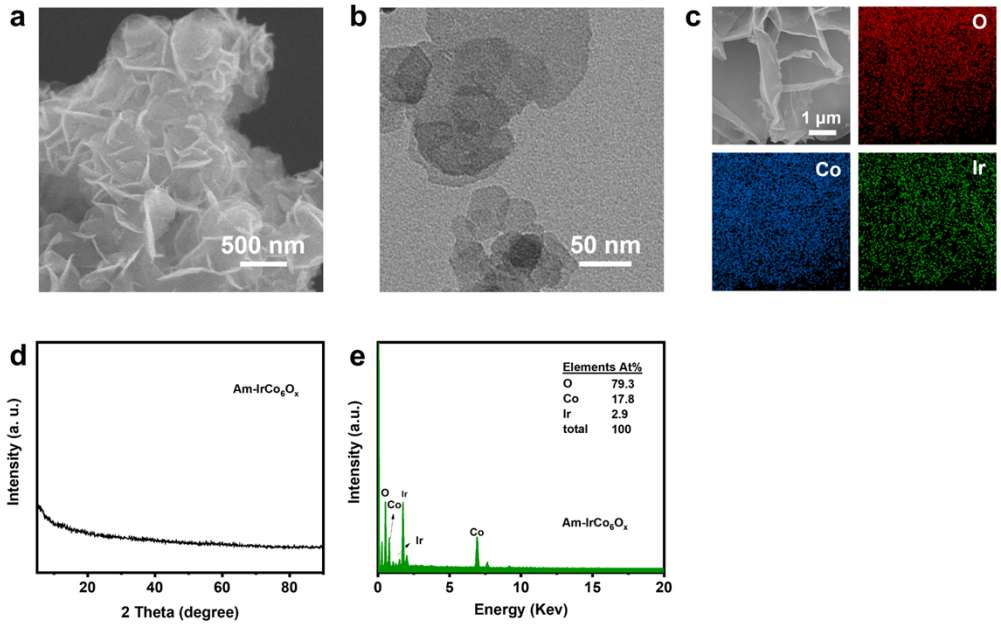

Figure S7. (a) SEM image of Am-$IrCo_6O_x$. (b) TEM image of Am-$IrCo_6$Ox. (c) STEM-EDS element mapping images of Am-$IrCo_6O_x$. (d) XRD pattern of Am-$IrCo_6O_x$. (e) EDS image of Am-$IrCo_6O_x$.

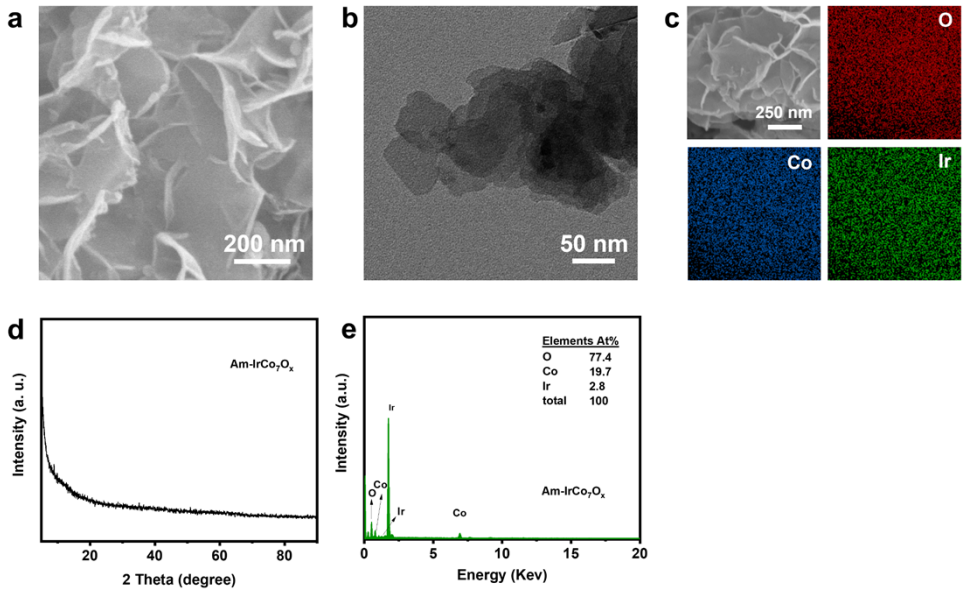

Figure S8. (a) SEM image of Am-$IrCo_7O_x$. (b) TEM image of Am-$IrCo_7O_x$. (c) STEM-EDS element mapping images of Am-$IrCo_7O_x$. (d) XRD pattern of Am-$IrCo_7O_x$. (e) EDS image of Am-$IrCo_7O_x$.

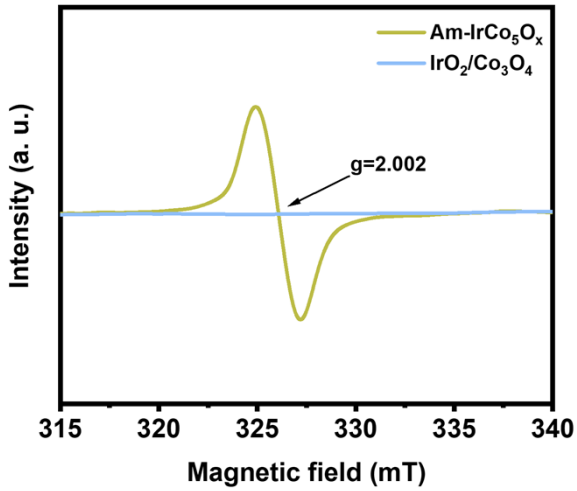

Figure S9. EPR spectra of Am-$IrCo_5O_x$ and IrO_2/Co_3O_4.

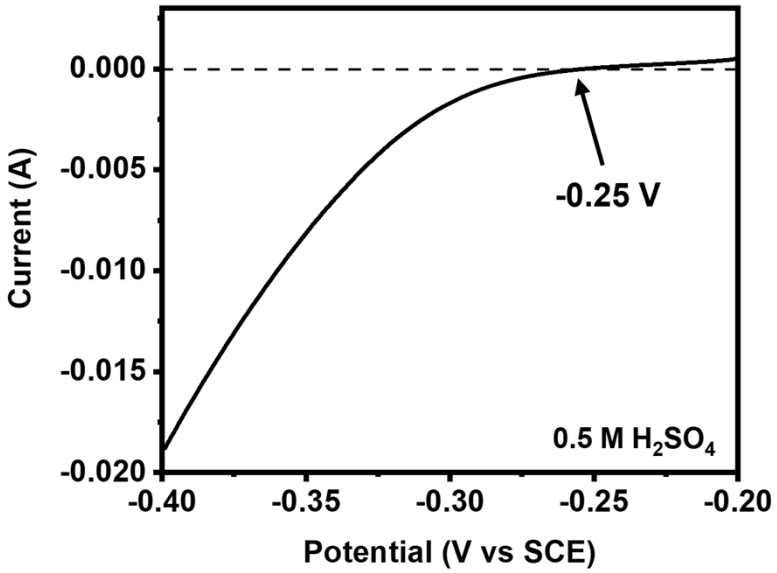

Figure S10. Calibration of the saturated calomel electrode (SCE) electrode with respect to reversible hydrogen electrode (RHE) in 0.5 M H_2SO_4 aqueous electrolytes bubbled with pure hydrogen gas at room temperature. Scan rate: 1 mV s^{-1}.

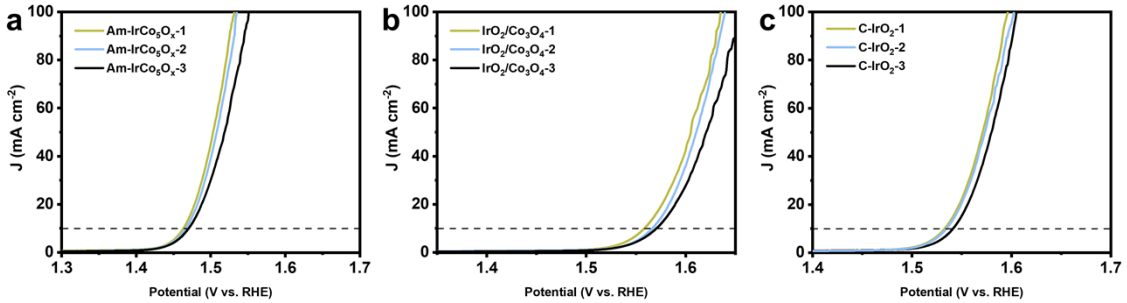

Figure S11. Reproducibility experiments for (A) Am-$IrCo_5O_x$, (b) IrO_2/Co_3O_4 and (c) C-IrO_2.

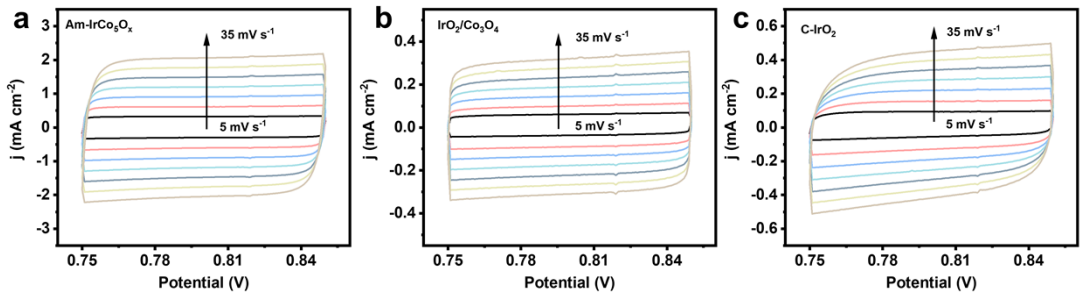

Figure S12. Measured CVs of (a) Am-$IrCo_5O_x$, (b) IrO_2/Co_3O_4 (c) IrO_2 in 0.5 M H_2SO_4 electrolyte with a potential range, measured at the scan rates of 5, 10, 15, 20, ,25, 30 and 35 mV s^{-1}. The current densities were obtained from the double layer charge/discharge curves.

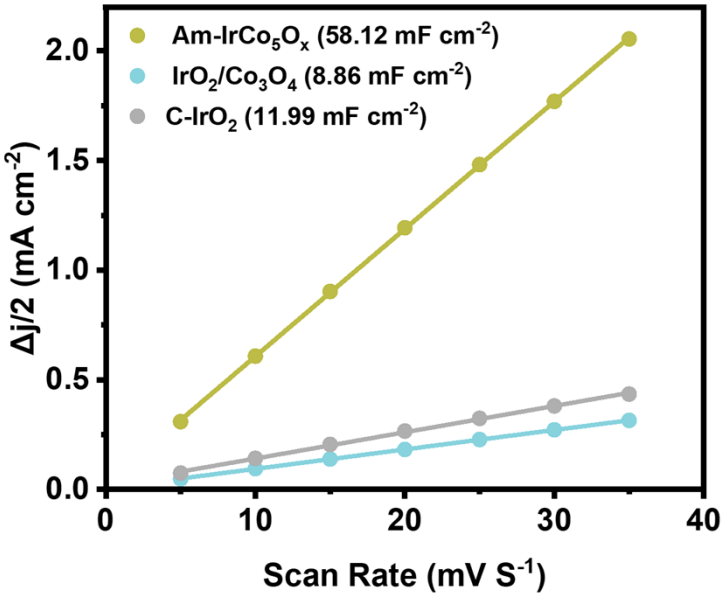

Figure S13. C_{dl} plots obtained from the polarization curves of Am-$IrCo_5O_x$, IrO_2/Co_3O_4 and C-IrO_2.

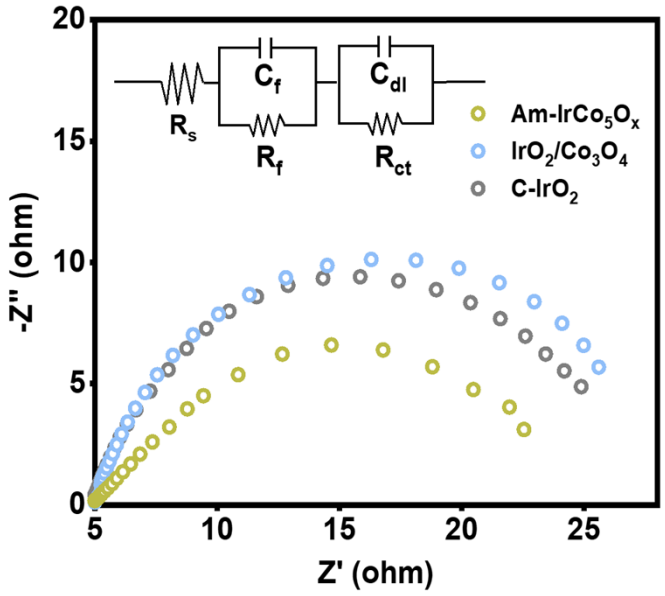

Figure S14. Nyquist diagrams of Am-$IrCo_5O_x$, IrO_2/Co_3O_4 and C-IrO_2. The curves were the fitting result using the equivalent circuit shown in the illustration.

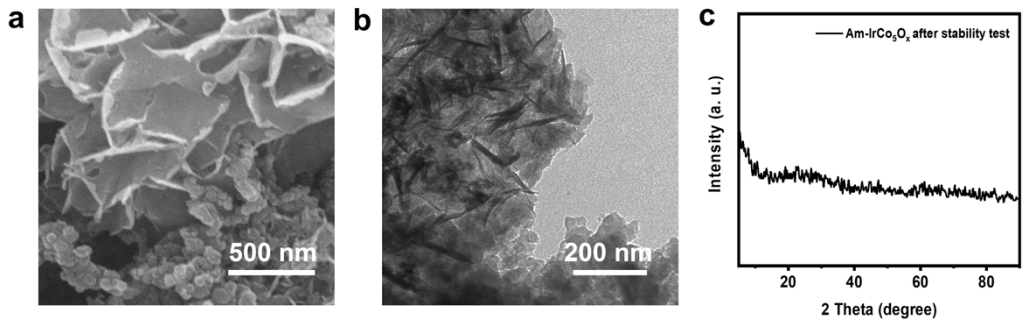

Figure S15. (a) SEM image and (b) TEM image of Am-$IrCo_5O_x$ after 122 hours stability test. (c) XRD of Am-$IrCo_5O_x$ after 122 hours stability test.

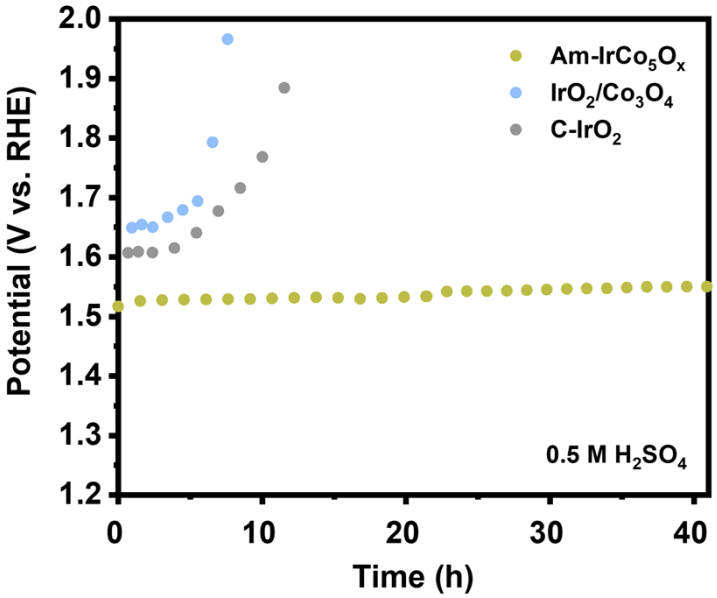

Figure S16. Chronopotentiometry test of Am-$IrCo_5O_x$, IrO_2/Co_3O_4 and C-IrO_2 at the current density of 50 mA cm^{-2}.

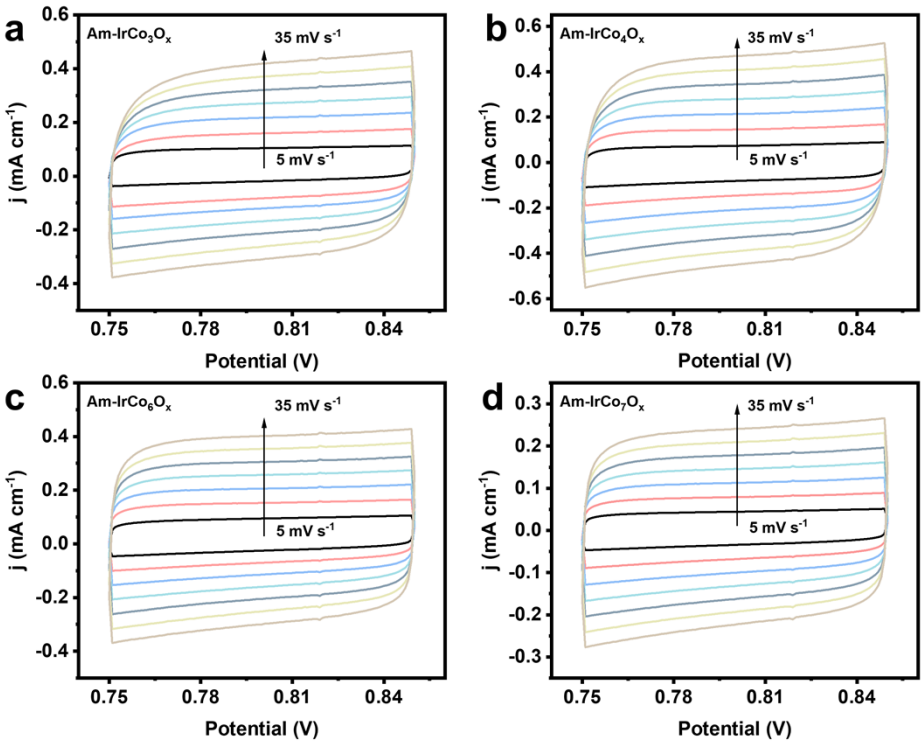

Figure S17. Measured CVs of (a) Am-$IrCo_3O_x$, (b) Am-$IrCo_4O_x$, (c) Am-$IrCo_6O_x$, (d) Am-$IrCo_7O_x$ in 0.5 M H_2SO_4 electrolyte with a potential range: 5, 10, 15, 20, 25, 30 and 35 mV s^{-1}. The current densities were obtained from the double layer charge/discharge curves.

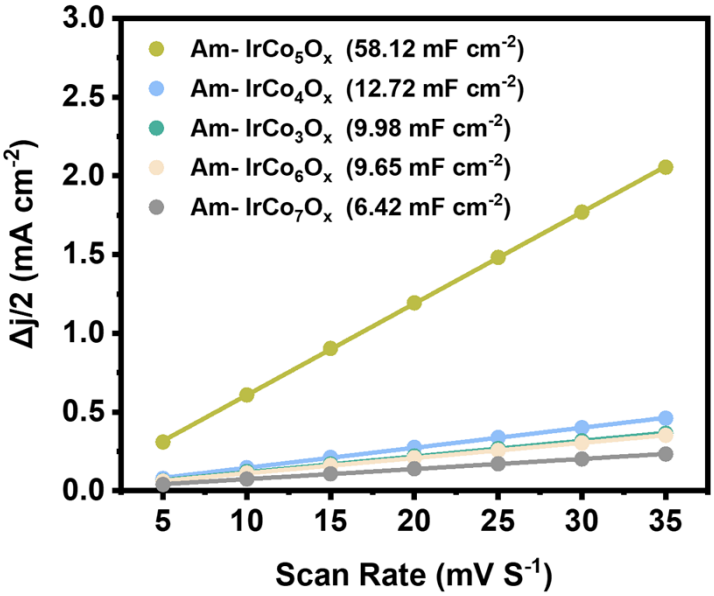

Figure S18. C_{dl} plots obtained from the polarization curves of Am-$IrCo_5O_x$, Am-$IrCo_3O_x$, Am-$IrCo_4O_x$, Am-$IrCo_6O_x$, and Am-$IrCo_7O_x$.

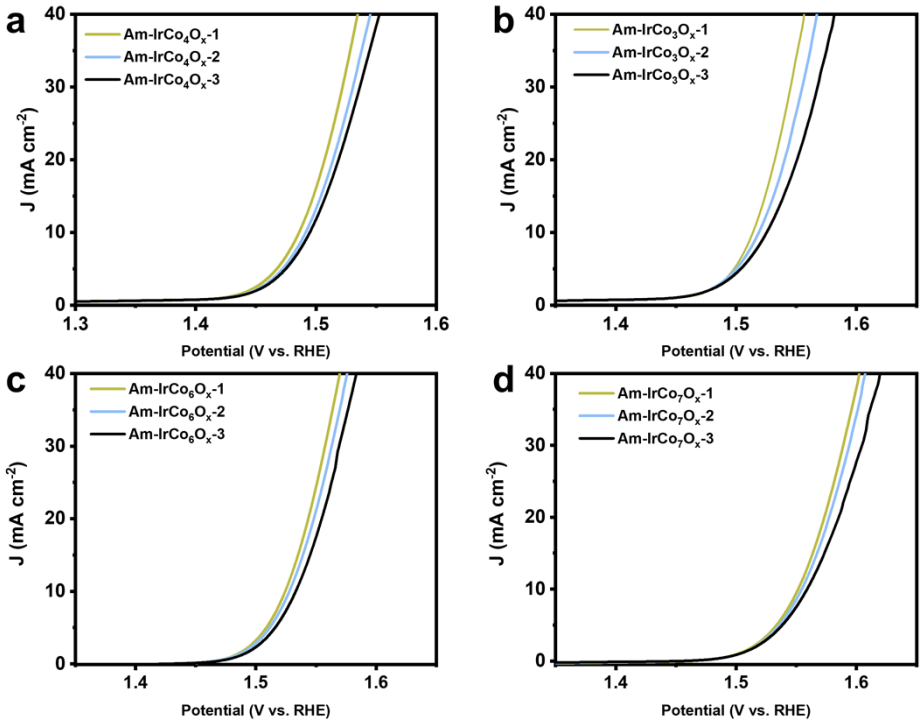

Figure S19. Reproducibility experiments for (A) Am-$IrCo_4O_x$, (b) Am-$IrCo_3O_x$, (c) Am-$IrCo_6O_x$ and (d) Am-$IrCo_7O_x$.

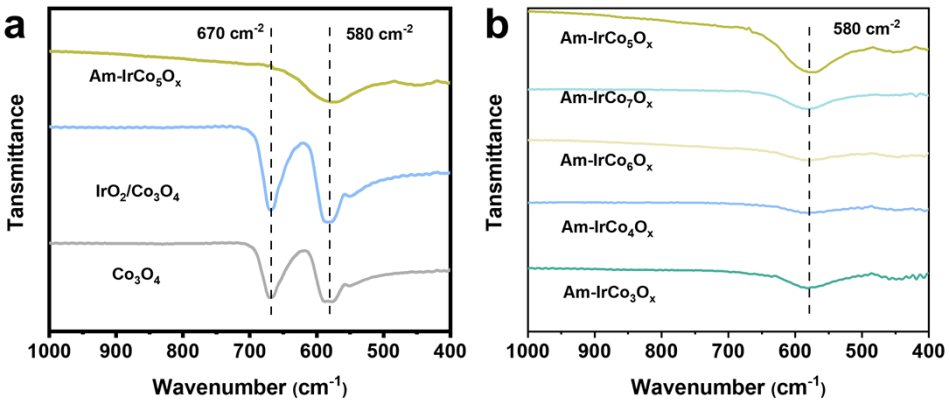

Figure S20. (a) The IR spectrum of Am-$IrCo_5O_x$, IrO_2/Co_3O_4, and Co_3O_4. (b) The IR spectrum of Am-$IrCo_5O_x$, Am-$IrCo_7O_x$, Am-$IrCo_6O_x$, Am-$IrCo_4O_x$, and Am-$IrCo_3O_x$.

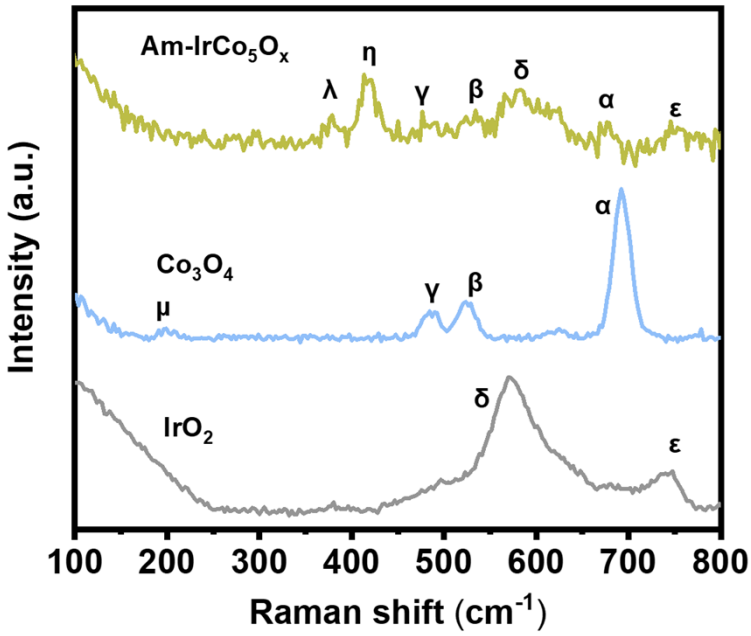

Figure S21. Raman of Am-$IrCo_5O_x$, Co_3O_4 and IrO_2.

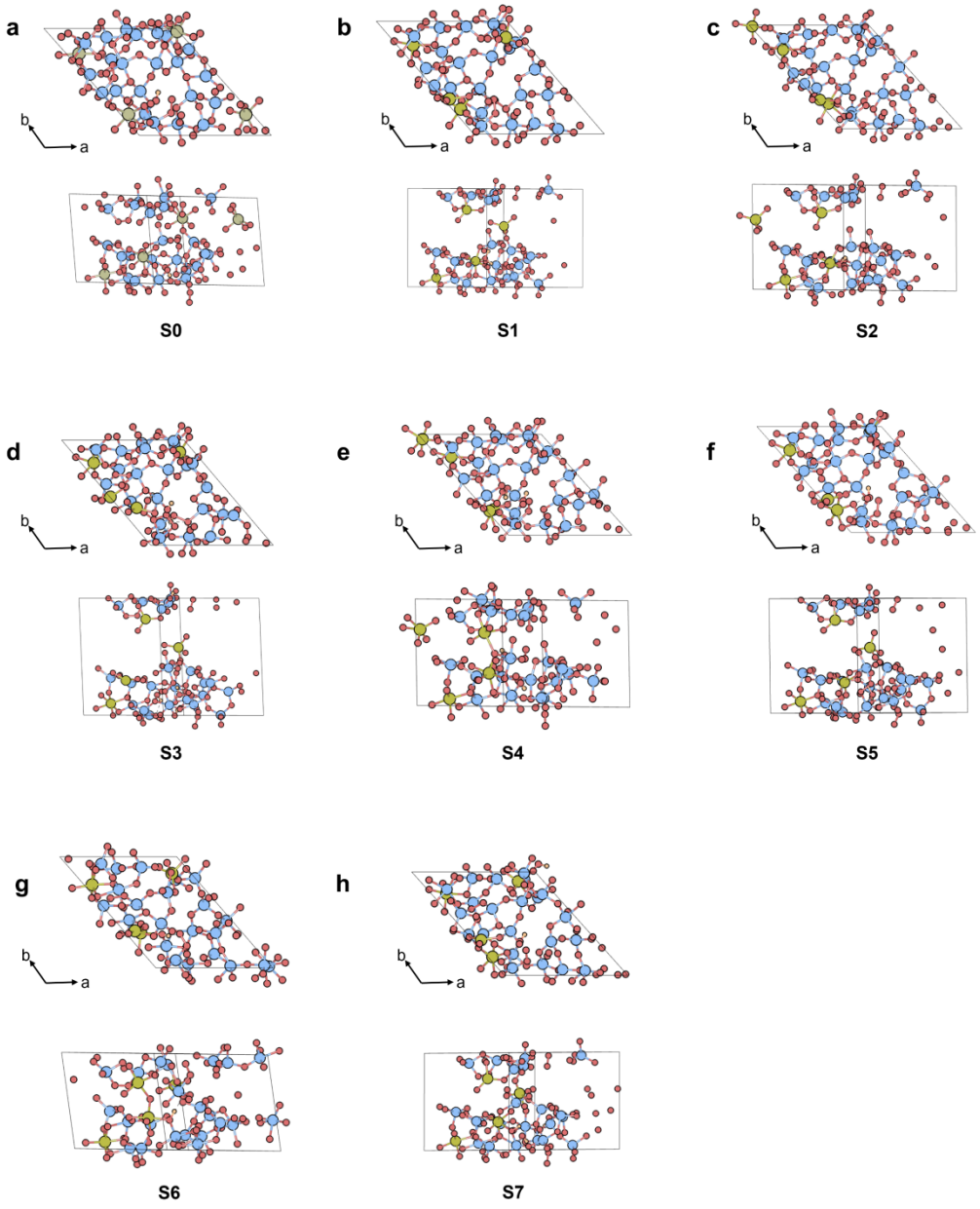

Figure S22. The optimized structures of all states for OER on Ir sites on Am-$IrCo_5O_x$.

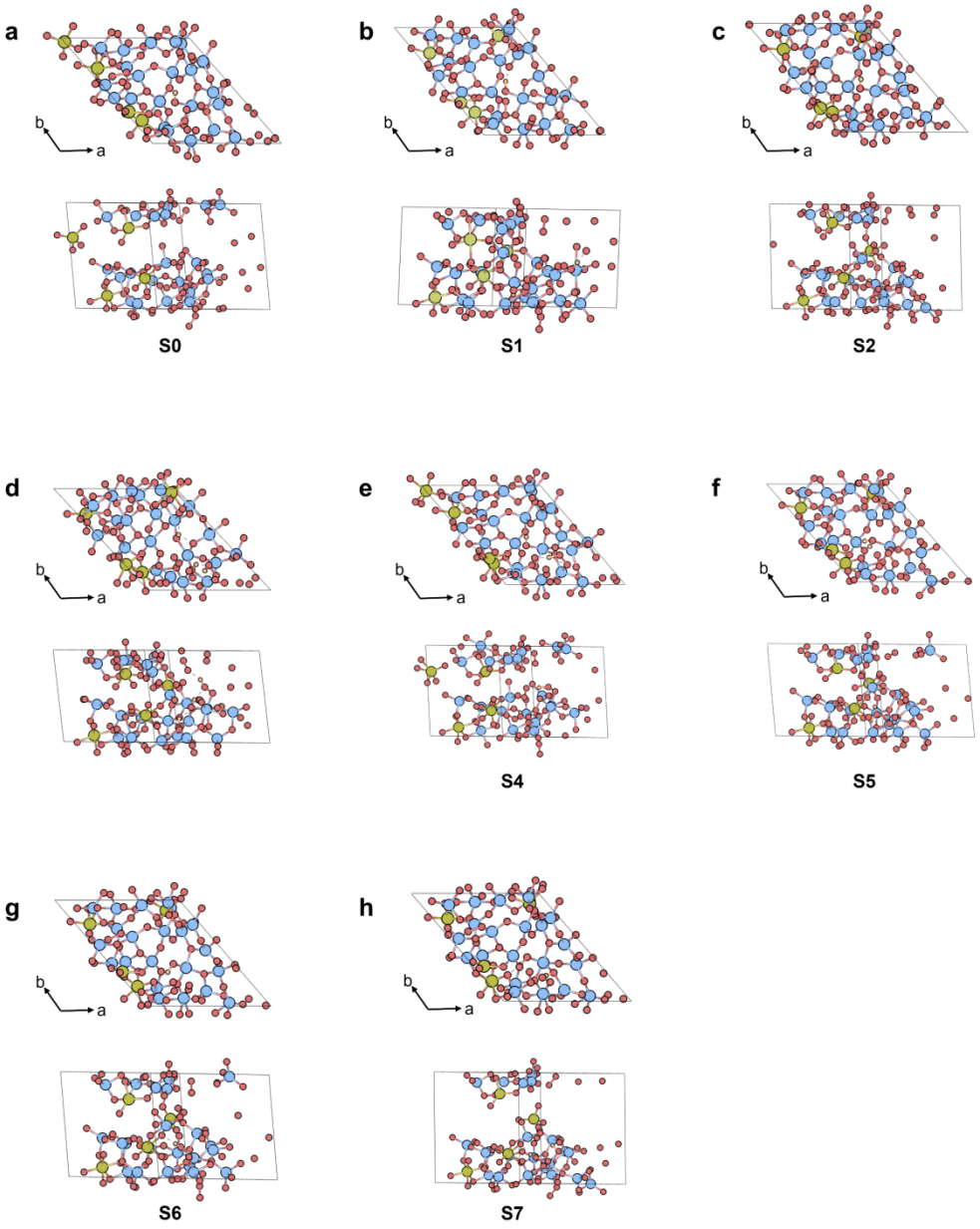

Figure S23. The optimized structures of all states for OER on Co sites on Am-$IrCo_5O_x$.

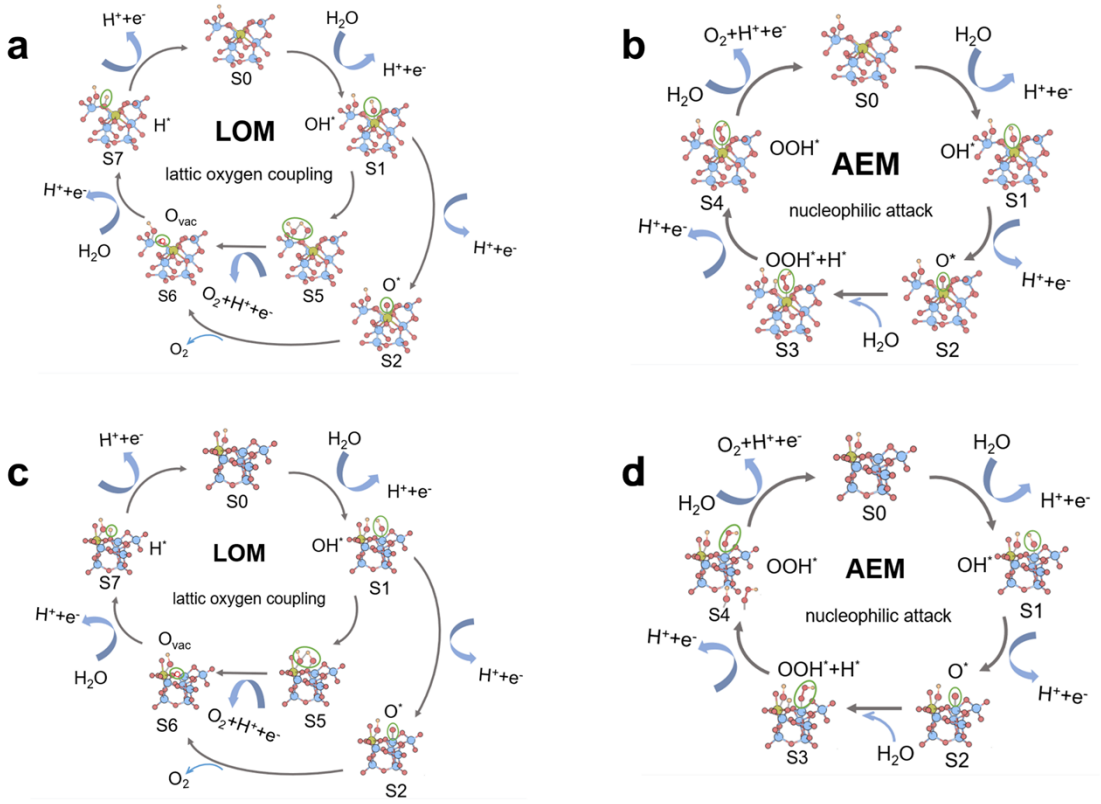

Figure. S24. Schematic representation of the OER mechanism on Ir sites on Am-$IrCo_5O_x$ surface: (a) LOM and (b) AEM. Schematic representation of the OER mechanism on Co sites on Am-$IrCo_5O_x$ surface: (c) LOM and (d) AEM.

Table S1. Comparisons of OER performance for various Ir-based electrocatalysts.

Catalysts	Electrolyte	Overpotential (mV @ 10 mA cm^{-2})	Tafel slope (mV dec^{-1})	Mass activity (A g_{Ir}^{-1})	Stability	Refs
Am-$IrCo_5O_x$	0.5 M H_2SO_4	230 mV	61.5	973.71 @ 1.53 V	150 h @ 10 mA cm^{-2}	This work
Ir/WO_3	0.5 M H_2SO_4	249 mV	71.1	/	36 h @ 10 mA cm^{-2}	1
KIr_4O_8	0.5 M H_2SO_4	266 mV	48.2	109.6 @ 1.53 V	100 h @ 10 mA cm^{-2}	2
IrY	0.5 M H_2SO_4	255 mV	54.8	96.3 @ 1.53 V	800 h @ 10 mA cm^{-2}	3
HEA@Ir-MEO	0.5 M H_2SO_4	243 mV	56.2	261.5 @ 1.55 V	24 h @ 10 mA cm^{-2}	4
Ir–Ce SSO	0.5 M H_2SO_4	238 mV	65.9	637.88 @ 1.55 V	100 h @ 10 mA cm^{-2}	5
0.2Mo-PIO-post	0.5 M H_2SO_4	265 mV	62.15	1216 @ 1.55 V	/	6
Ti-IrOx/Ir	0.5 M H_2SO_4	254 mV	48.0	338 @ 1.58 V	100 h @ 10 mA cm^{-2}	7
ZnNiCoIrMn	0.1 M $HClO_4$	237 mV	46	675.3 @ 1.5 V	100 h @ 10 mA cm^{-2}	8
Ir-Co_3O_4	0.5 M H_2SO_4	236 mV	52.6	3343.37 @ 1.53 V	30 h @ 100 mA cm^{-2}	9
La_3IrO_7-SLD	0.1 M $HClO_4$	296 mV	52	~250 @	60000 S @	10

				1.60 V	10 mA cm^{-2}	
IrW-W_2B	0.5 M H_2SO_4	291 mV	78	/	120 h @ 100 mA cm^{-2}	11
D-$IrTe_2$ HNSs	0.5 M H_2SO_4	298 mV	49.4	213.8 @ 1.5 V	10000 S @ 10 mA cm^{-2}	12
Li–IrO_x	0.5 M H_2SO_4	300 mV	39	100 @ 1.52 V	10 h @ 10 mA cm^{-2}	13
6H-$SrIrO_3$	0.5 M H_2SO_4	245 mV	/	~75 @1.525 V	30 h @ 10 mA cm^{-2}	14

Table S2. ICP-MS test of Am-$IrCo_5O_x$ during the 122 hours long-term stability test to check the concentration of dissolved Ir and Co in the electrolyte.

Time (h)	Dissolved cobalt after stability test at 10 mA cm^{-2} (μg_{Co} mL^{-1})	Dissolved iridium after stability test at 10 mA cm^{-2} (μg_{Ir} mL^{-1})
1	1.41	0.16
10	1.79	0.22
20	1.88	0.28
40	2.26	0.40
60	2.47	0.44
80	2.56	0.46
100	2.61	0.48
122	2.76	0.58

Table S3. Comparison of overpotential of catalysts with different ratios of Ir and Co.

Catalysts	Am-$IrCo_5O_x$	Am-$IrCo_4O_x$	Am-$IrCo_3O_x$	Am-$IrCo_6O_x$	Am-$IrCo_7O_x$
Overpotential (mV @ 10 mA cm^{-2})	230 mV	253 mV	280 mV	292 mV	317 mV

Table S4. Grand free energy of mechanistic reactions steps under different reaction mechanisms on Ir sites on Am-$IrCo_5O_x$.

Reaction	ΔG (eV)
$S0+H_2O \rightarrow S1+H^+ + e^-$	0.21
$S1 \rightarrow S2+H^+ + e^-$	-0.16
$S2+H_2O \rightarrow S3$	0.53
$S3 \rightarrow S4+ H^+ + e^-$	-0.17
$S4+ H_2O \rightarrow S0+O_2+H^+ + e^-$	-0.40
$S1 \rightarrow S5$	0.12
$S5 \rightarrow S6+O_2+H^+ + e^-$	0.09
$S6+ H_2O \rightarrow S7+H^+ + e^-$	-0.56
$S7 \rightarrow S0+H^+ + e^-$	0.14

Table S5. Grand free energy of mechanistic reactions steps under different reaction mechanisms on Co sites on Am-$IrCo_5O_x$.

Reaction	ΔG (eV)
$S0+H_2O \rightarrow S1+H^+ + e^-$	1.64
$S1 \rightarrow S2+H^+ + e^-$	-1.43
$S2+H_2O \rightarrow S3$	-0.96
$S3 \rightarrow S4+H^+ + e^-$	1.67
$S4+ H_2O \rightarrow S0+O_2+H^+ + e^-$	-0.92
$S1 \rightarrow S5$	0.58
$S5 \rightarrow S6+O_2+H^+ + e^-$	-2.43
$S6+ H_2O \rightarrow S7+H^+ + e^-$	0.90
$S7 \rightarrow S0+H^+ + e^-$	-0.70

Reference

1 W. Wang, C. Li, C. Zhou, X. Xiao, F. Li, N. Huang, L. Li, M. Gu and Q. Xu, *Angew. Chem. Int. Ed.*, 2024, **63**, e202406947.

2 Z. Li, X. Li, M. Wang, Q. Wang, P. Wei, S. Jana, Z. Liao, J. Yu, F. Lu, T. Liu and G. Wang, *Adv. Mater.*, 2024, **36**, 2402643.

3 X. Xiong, J. Tang, Y. Ji, W. Xue, H. Wang, C. Liu, H. Zeng, Y. Dai, H. Peng, T. Zheng, C. Xia, X. Liu and Q. Jiang, *Adv. Energy Mater.*, 2024, **14**, 2304479.

4 L. Yao, F. Zhang, S. Yang, H. Zhang, Y. Li, C. Yang, H. Yang and Q. Cheng, *Adv. Mater.* 2024, **36**, 2314049.

5 Z. Dong, C. Zhou, W. Chen, F. Lin, H. Luo, Z. Sun, Q. Huang, R. Zeng, Y. Tan, Z. Xiao, H. Huang, K. Wang, M. Luo, F. Lv and S. Guo, *Adv. Funct. Mater.*, 2024, 2400809.

6 S. Chen, S. Zhang, L. Guo, L. Pan, C. Shi, X. Zhang, Z.-F. Huang, G. Yang and J.-J. Zou, *Nat. Commun.*, 2023, **14**, 4127.

7 Y. Wang, R. Ma, Z. Shi, H. Wu, S. Hou, Y. Wang, C. Liu, J. Ge and W. Xing, *Chem*, 2023, **9**, 2931–2942.

8 J. Kwon, S. Sun, S. Choi, K. Lee, S. Jo, K. Park, Y. K. Kim, H. B. Park, H. Y. Park, J. H. Jang, H. Han, U. Paik and T. Song, *Adv. Mater.*, 2023, **35**, 2300091.

9 Y. Zhu, J. Wang, T. Koketsu, M. Kroschel, J.-M. Chen, S.-Y. Hsu, G. Henkelman, Z. Hu, P. Strasser and J. Ma, *Nat. Commun.*, 2022, **13**, 7754.

10 Q. Qin, H. Jang, Y. Wang, L. Zhang, Z. Li, M. G. Kim, S. Liu, X. Liu and J. Cho, *Adv. Energy Mater.*, 2021, **11**, 2003561.

11 R. Li, H. Wang, F. Hu, K. C. Chan, X. Liu, Z. Lu, J. Wang, Z. Li, L. Zeng, Y. Li, X. Wu and Y. Xiong, *Nat. Commun.*, 2021, **12**, 3540.

12 Y. Pi, Y. Xu, L. Li, T. Sun, B. Huang, L. Bu, Y. Ma, Z. Hu, C. Pao and X. Huang, *Adv. Funct Mate.*, 2020, **30**, 2004375.

13 J. Gao, C.-Q. Xu, S.-F. Hung, W. Liu, W. Cai, Z. Zeng, C. Jia, H. M. Chen, H. Xiao, J. Li, Y. Huang and B. Liu, *J. Am. Chem. Soc.*, 2019, **141**, 3014–3023.

14 L. Yang, G. Yu, X. Ai, W. Yan, H. Duan, W. Chen, X. Li, T. Wang, C. Zhang, X. Huang, J.-S. Chen and X. Zou, *Nat. Commun.*, 2018, **9**, 5236.